Effect of Combustion Chamber Design on Performance of Magnesium-Loaded HTPB/N2O Hybrid Rocket for Spacecraft

By Tomoya KANDA,[1] Keita NISHII, [1] and Akira KAKAMI[1]

[1]Department of Aeronautics and Astronautics, Tokyo-Metropolitan University, Tokyo, Japan

This study investigated combustion chamber design effects on a small satellite hybrid thruster using Mg-added HTPB fuel and N_2O oxidizer. While Mg can enhance fuel regression and density specific impulse, it also increases combustion residue and nozzle clogging. The research aimed to determine how characteristic length (L*) influences characteristic velocity (C*) efficiency with Mg-added fuel, and how nozzle geometry affects residue removal. Combustion tests used three chamber types: rectangular nozzles with L* of 1.9 m and 3.7m, and a convergent nozzle (L*=1.9 m), varying Mg addition (0%, 20%, 40% by weight). The results showed that increasing L* improved mass utilization efficiency and suppressed the accumulation of combustion residue in the combustion chamber. However, nozzle geometry had no clear effect on residue expulsion. Theoretically, density specific impulse improves with Mg addition, but experiments revealed a decrease in density specific impulse in some combustion chambers, especially at 40% Mg addition. This finding suggests that to improve the performance of Mg-added hybrid thrusters, it is crucial to ensure a sufficient combustion chamber volume to accommodate combustion residue and to prevent residue from adhering near the nozzle throat.

Key Words: Propulsion, Fuels, Magnesium, Combustion residues, Hybrid thruster

Nomenclature

P_c	:	combustion chamber pressure, MPa
ε	:	area ratio, -
C^*	:	characteristic exhaust velocity, m/s
L^*	:	characteristic length, m
F	:	thrust, N
A_t	:	throat diameter, mm
C_F	:	thrust coefficient
$\dot{m}$	:	mass flow rate, g/s
I_{sp}	:	specific impulse, s
I	:	total impulse, Ns
g	:	gravitational acceleration, m/s^2
Δm	:	consumed mass, g
t	:	time, s
$\dot{r}$	:	fuel regression rate, mm/s
D	:	fuel grain inner diameter, mm
ρ	:	density, g/cm^3
L	:	length, mm
Subscripts		
i	:	initial combustion phase
d	:	design value
th	:	theoretical value
f	:	fuel grain
ox	:	oxidizer
res	:	combustion residue
0	:	end of combustion
b	:	start of combustion

1. Introduction

In recent years, the number of small satellite launches has been increasing[1]. For these satellite launches, a rideshare method is predominant, where multiple satellites are loaded onto a single rocket and simultaneously injected into the same orbit[2]. A challenge with this method is that each satellite may not be separated at its optimal position. However, by equipping satellites with propulsion systems, it becomes possible to inject them into their required orbits.

Traditionally, liquid propulsion systems have been widely used for satellites. However, their complex structure and the toxicity of hydrazine propellants pose challenges in terms of safety and management costs for small satellite applications. Particularly, with the current trend of small satellite development being led by universities and startup companies, there is a strong demand to resolve these issues. Against this backdrop, we have focused on incorporating hybrid rocket engines into small satellites, referred to as hybrid thrusters.

Hybrid thrusters offer high safety due to the separate storage of fuel grain and oxidizer, as well as the low toxicity of their propellants. Compared to liquid propulsion systems, they handle only one type of liquid, allowing for a reduction in components such as tanks and valves, resulting in a simpler structure. Furthermore, the ease of controlling oxidizer flow enables thrust control and re-ignition, making them advantageous. Therefore, they are effective propulsion systems suitable for small satellites. Given the high demand for miniaturization in small satellites, this study hypothesized that adding magnesium (Mg) to the fuel grain of hybrid thrusters could enhance the fuel grain's energy density, thereby enabling the overall miniaturization of the propulsion system.

This study focuse on hybrid thrusters using nitrous oxide (N_2O) as the oxidizer and hydroxyl-terminated polybutadiene (HTPB) with added micro-sized magnesium (Mg) as the fuel grain. N_2O is non-toxic and environmentally friendly. It's also

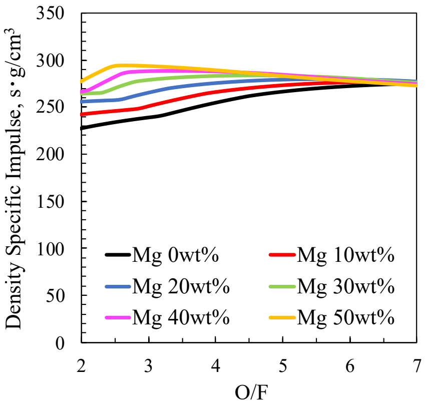

Fig. 1. Theoretical density specific impulse (Calculation conditions: equilibrium flow, P_c=0.4 MPa, ε=50).

highly effective as an oxidizer because its self-vapor pressure allows for oxidizer supply without the need for an additional pressurization device. In addition, HTPB has been widely adopted as a fuel grain component in solid rockets.

Previous research has explored various attempts to improve hybrid rocket performance by adding metal particles to the fuel grain. Among these, many studies have focused on aluminum (Al). Al is known to form a protective oxide layer at high temperatures, making it difficult to ignite[3]. In contrast, Mg's oxide layer is not protective, and it's easier to ignite compared to Al, which led to its selection for this study[3].

Two effects are expected from Mg addition in this research. The first is an improvement in fuel regression rate. An increased fuel regression rate leads to a higher fuel grain mass flow rate, which enables higher thrust from a smaller propulsion system. Indeed, there are prior studies confirming an increase in fuel regression rate with the addition of 10wt% micro-sized Mg particles[4]. However, no prior research on Mg addition has been confirmed under the low combustion chamber pressure and low oxidizer flow rate conditions targeted in this study. The second expected effect is an improvement in density specific impulse. The theoretical density specific impulse calculated by NASA-CEA[5] is shown in Fig. 1. Figure 1 indicates that the density specific impulse increases as the Mg addition ratio to HTPB increases.

We developed a 1 N-class single-port hybrid thruster prototype and conducted combustion experiments by varying the Mg addition ratio to HTPB (0, 10, 20, 23, 40, and 50 wt%)[6]. A cross-sectional view of the thruster is shown in Fig. 2. This hybrid thruster features a small fuel grain size and is equipped with a post-combustion chamber to ensure sufficient residence time for combustion gases. Figure 3 shows the relationship between oxidizer mass flux and fuel regression rate for each Mg addition ratio. Notably, the addition of Mg has a noticeable effect on the fuel regression rate.

In the post-combustion chamber, we observed an increase in combustion residue as the Mg addition ratio increased. Figure 4 shows the appearance of the post-combustion chamber for HTPB 100 wt% and Mg 50 wt% at the same oxidizer flow rate. As shown in Fig. 4, while the HTPB 100 wt% case showed only a thin layer of soot covering the walls,

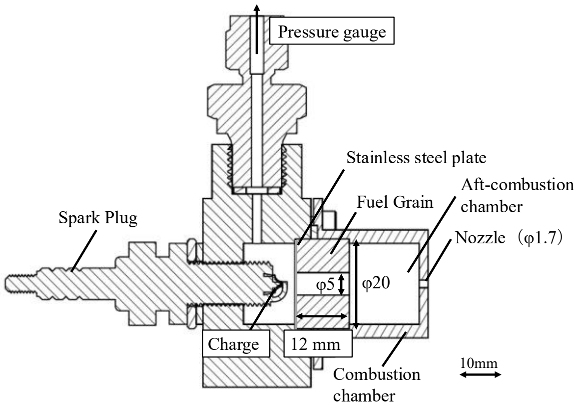

Fig. 2. Cross-sectional view of the thruster.

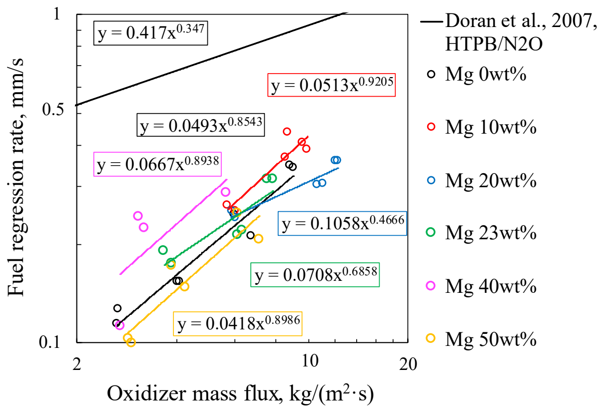

Fig. 3. Fuel regression rate vs. oxidizer mass flux.

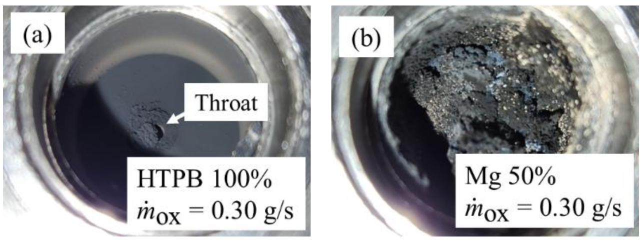

Fig. 4. Appearance of the post-combustion chamber.

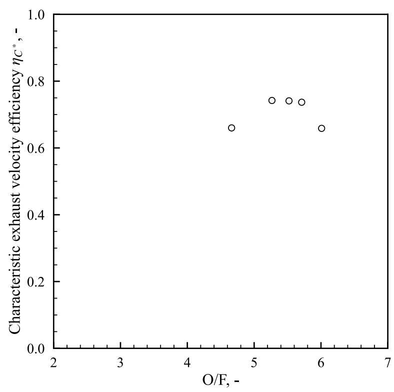

Fig. 5. C* efficiency vs. O/F (HTPB 100wt%).

the Mg 50 wt% case exhibited a large amount of combustion residue that obscured the bottom. This combustion residue is problematic as it can cause nozzle clogging, leading to performance degradation such as thrust reduction.

Furthermore, Fig. 5 shows the $C*$ efficiency calculated from combustion chamber pressure measurements for 100 wt% HTPB fuel grain. The C^* efficiency of this hybrid hruster, with a design L^* of 1.9 m (including the post-combustion chamber), tended to be low at 71.1 ± 3.7%. This low efficiency could be attributed to insufficient L^* and significant heat loss from the post-combustion chamber.

While Mg addition promises improved fuel regression rate and density specific impulse, it also brings notable challenges. Specifically, two sets of issues arise: These fall into two main categories: those arising directly from Mg addition, such as potential performance degradation due to combustion residue accumulation and difficulties in performance evaluation from nozzle clogging; and those inherent to the hybrid thruster itself, including the relatively low C^* efficiency observed with 100 wt% HTPB fuel grain. As described, Mg addition has the potential to enhance fuel regression rate and density specific impulse, yet it presents several challenges. These include potential performance degradation from combustion residue buildup and difficulties in assessing performance due to nozzle clogging. The hybrid thruster also has its own challenge of relatively low C^* efficiency with 100 wt% HTPB fuel grain.

Based on the issues identified in the aforementioned prior research, this study has two research objectives. The first objective is to investigate the effect of characteristic length L^* on combustion efficiency, particularly when using Mg-added fuel grain. To address the low C^* efficiency suggested in previous studies with pure HTPB fuel grain, L^* will be used as a parameter (specifically, combustion chambers with L^* = 1.9 m and L^* = 3.7 m) to quantitatively evaluate C^* efficiency. Combustion chamber pressure and thrust measurement results will be used to calculate C* efficiency. The effectiveness of increasing L^* as a measure to improve combustion efficiency will be examined. The second objective is to clarify the relationship between nozzle geometry and combustion residue expulsion. To address the problem of large amounts of combustion residue occurring when using Mg-added fuel grain, the effect of nozzle geometry on residue expulsion will be investigated. Specifically, combustion experiments will be conducted using rectangular nozzles and convergent nozzles to quantitatively evaluate the amount of combustion residue. The aim is to clarify the effectiveness of nozzle geometry as a measure to reduce combustion residue.

2. Methods

2.1. Experimental Setup

2.1.1. 1 N-class hybrid thruster

In this study, a 1 N-class hybrid thruster was fabricated, and combustion tests were conducted. This single-port hybrid thruster utilizes N_2O as the oxidizer and Mg-added HTPB as the fuel grain. Figure 6 shows a CAD drawing of the thruster, specifically illustrating the combustion chamber with an L^* of 1.9 m. Figure 7 displays an external view photo of the fuel grain. The thruster's specifications are summarized in Table 1. To prevent burning of the fuel grain end face, a 0.1 mm thick stainless-steel plate is placed on its upstream side. The Mg particle size is 149 μm or less.

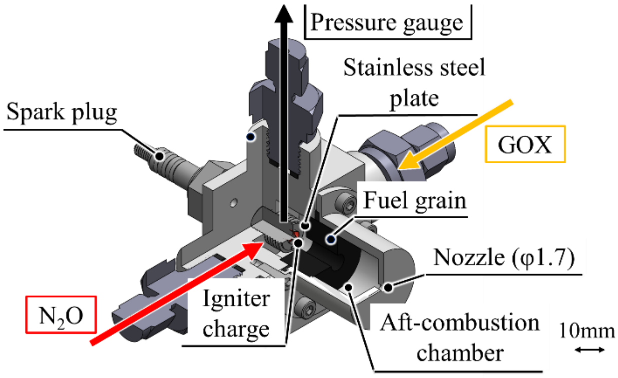

Fig. 6. 1 N-class hybrid thruster.

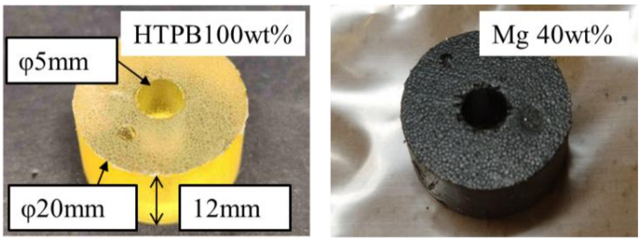

Fig. 7. Fuel grain (HTPB 100wt%, Mg 40wt%).

Table 1. Thruster Parameters.

Thruster materials	SUS303
Target thrust, N	1.0
Target thrust chamber pressure, MPa	0.4
Throat diameter, mm	1.7
Nozzle area ratio, -	1
Fuel Dimensions, mm (Inner diameter / Outer diameter / Height)	φ5/φ20/12

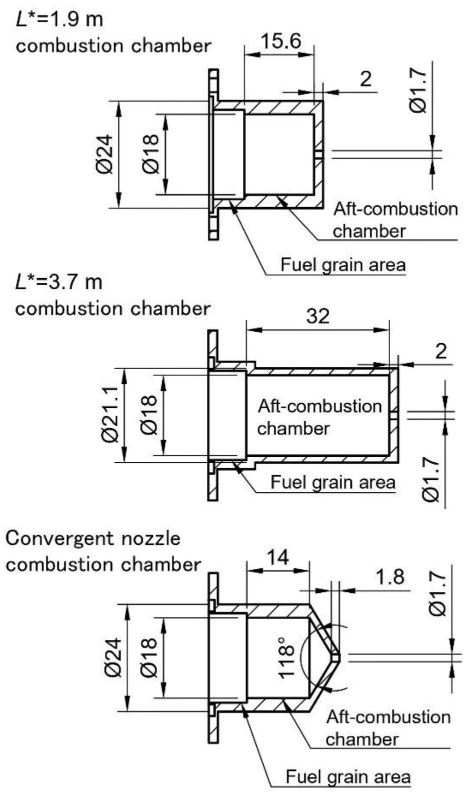

Fig. 8. Cross-sectional views of the three types of combustion chambers.

3

In this study, experiments were conducted using three types of combustion chamber geometries to investigate the effect of L^* on combustion efficiency and the effect of nozzle geometry on combustion residue expulsion. The combustion chambers used were the L^* = 1.9 m combustion chamber, the L^* = 3.7 m combustion chamber, and the convergent nozzle combustion chamber. Cross-sectional views are shown in Fig. 8. The L^* = 1.9 m combustion chamber and the L^* = 3.7 m combustion chamber are rectangular nozzles without a convergent section. Conversely, the convergent nozzle combustion chamber is equipped with a convergent nozzle with a tip angle of 118°. The L^* of the convergent nozzle combustion chamber corresponds to 1.9 m. The volume of the post-combustion chamber wall was identical for all three combustion chambers.

2.1.2. Ignition system

Ignition of the hybrid thruster in this study was achieved using a spark plug. An igniter charge, serving as a flame source, was attached to the tip of the spark plug. This igniter charge was fabricated by a stereolithography 3D printer using Formlabs Clear Resin v4. Its mass is 0.02 g, and its influence was disregarded during performance evaluation.

Since it was difficult to ignite the fuel grain with N_2O alone as the oxidizer, gaseous oxygen (GOX) was supplied in addition to N_2O during ignition to assist in the process.

During the experiments, the operation of the spark plug could not be visually confirmed. Therefore, current and voltage waveforms were recorded using an oscilloscope.

2.1.3. Oxidizer feed system

Figure 9 shows a schematic diagram of the oxidizer feed system used in this study. The oxidizer feed system is responsible for supplying N_2O and GOX to the thruster. The feed system mainly consists of a regulator, a solenoid valve, a mass flow controller, and a check valve. In this study, the supply pressure was set to 0.6 MPa. The oxidizer flow rate was controlled by a mass flow controller (KOFLOC, MODEL 3660 SERIES).

2.1.4. Measurement system

For performance evaluation in this study, combustion chamber pressure and thrust were measured. A pressure transducer was installed upstream of the fuel grain, as shown in Fig. 6. For thrust measurement, a vertical pendulum-type thrust stand was used, and thrust was calculated using a laser displacement sensor with a resolution of 0.5 µm. An eddy current damper was provided to suppress unwanted vibrations. A CAD drawing of the thrust stand is shown in Fig. 10. A load cell was used for calibration to convert displacement to thrust. Calibration was performed before each combustion experiment, confirming that the relationship between displacement and thrust could be linearly approximated with a coefficient of determination, R^2, of 0.999.

2.2. Experimental conditions

Table 2 shows the experimental conditions implemented in this study. In these experiments, the Mg additive ratio in the fuel and the combustion chamber geometry were set as parameters.

Table 3 presents the combinations of the Mg additive ratio and combustion chamber geometry, along with the number of experiments conducted for each condition. To confirm reproducibility, each condition was tested a minimum of two times. The reference combustion chamber with L^* = 1.9 m was tested three times for all conditions.

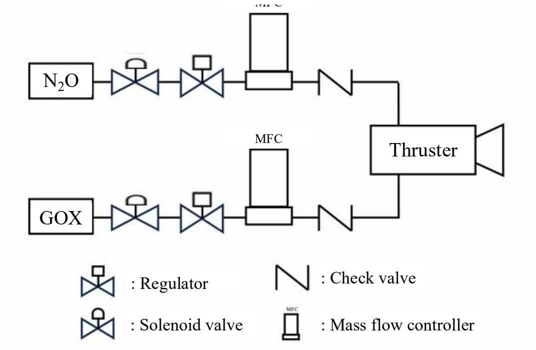

Fig. 9. Schematic diagram of the oxidizer feed system.

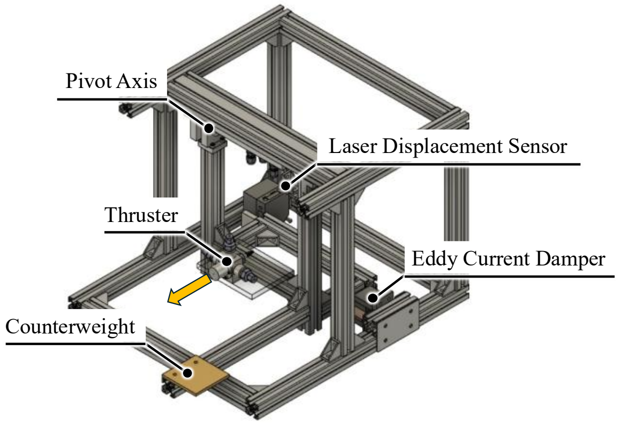

Fig. 10. Vertical pendulum-type thrust stand.

Table 2. Experimental conditions.

Fuel grain	Mg 0wt%, 20wt%, 40wt%
Oxidizer	N_2O
Oxidizer flow rate, g/s	0.46
Ignition gas flow rate, g/s	0.11
Target burn time, s	10
Atmosphere	Atmospheric pressure

Table 3. Combinations of Mg additive ratio and combustion chamber geometry, and number of experiments.

	L^*=1.9 m	L^*=3.7 m	Convergent nozzle
Mg 0wt%	3	2	2
Mg 20wt%	3	2	2
Mg 40wt%	3	2	2

2.3. Experimental Procedure

The combustion sequence proceeded as follows:

1. Supply of N_2O and GOX was initiated.
2. Spark plug voltage was applied to generate a spark.
3. Once flame discharge from the nozzle was confirmed via footage from the imaging equipment, the spark plug voltage was turned off, and GOX supply was stopped.
4. 10 seconds after the GOX supply stopped, the N_2O supply was terminated, concluding the combustion experiment.

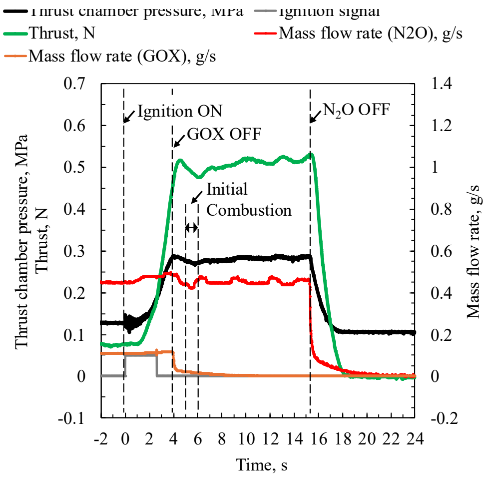

Fig. 11. Time-history of Combustion experiment.

Figure 11 shows the combustion chamber pressure, thrust, mass flow rates of N_2O and GOX, and the spark plug voltage application timing for the condition with 0 wt% Mg and L^* = 1.9 m combustion chamber. The origin of the time is set to the moment the voltage application to the spark plug began. In this experiment, N_2O and GOX were supplied simultaneously for approximately 4 seconds. GOX supply was stopped after approximately 4 seconds, and N_2O supply was stopped approximately 15 seconds later. For the N_2O mass flow rate, a mass flow controller performed flow control, and the N_2O supply was slightly affected by downstream pressure fluctuations.

2.4. Date analysis

In this study's combustion experiments, time-history data of combustion chamber pressure and thrust were acquired. The mass flow rates of N_2O and GOX were based on values controlled by mass flow controllers. Additionally, fuel consumption was calculated by measuring the difference in fuel mass before and after combustion. The start time of combustion was defined as when the maximum combustion chamber pressure reached 75%, and the end time of combustion was defined as when the N_2O gas supply was terminated. Based on these acquired data and measured values, the following propulsion performance indicators were calculated:

2.4.1. Nozzle efficiency

Equation (1) shows the calculation formula for the thrust coefficient (C_F) during the initial phase of combustion. In this analysis, the initial phase of combustion was defined as the 1-second period starting from when the GOX mass flow controller's flow rate decreased to 20% of its set value (0.11 g/s) after receiving the stop signal.

$$C_{F,\mathrm{i}} = \frac{F_\mathrm{i}}{P_{c,\mathrm{i}} A_{t,\mathrm{d}}} \tag{1}$$

Equation (2) shows the calculation formula for the nozzle efficiency. $C_{F,\mathrm{th}}$ was calculated for each experiment using NASA-CEA.

$$\eta_\mathrm{n} = \frac{C_{F,\mathrm{i}}}{C_{F,\mathrm{th}}} \tag{2}$$

2.4.2. *C**

Equation (3) shows the calculation formula for C^*. Typically, C^* is calculated using pressure, as shown in Eq. (4). However, in this study, nozzle clogging occurred when Mg was added, making it impossible to calculate the throat diameter during combustion. Therefore, we use the formula involving thrust, as presented in Eq. (4). Furthermore, the C_F inherently fluctuates during combustion due to changes in the flow inside the nozzle caused by nozzle clogging and combustion residues. However, in this analysis, we assume that C_F does not fluctuate during combustion.

$$C^* = \frac{\overline{F}}{C_{F,\mathrm{i}}\left(\overline{\dot{m}}_\mathrm{f} + \overline{\dot{m}}_\mathrm{ox}\right)} \tag{3}$$

$$C^* = \frac{P_c A_t}{\dot{m}_\mathrm{f} + \dot{m}_\mathrm{ox}} \tag{4}$$

2.4.3 Specific impulse

Specific impulse is defined by Eq. (5).

$$I_{sp} = \frac{I}{\mathrm{g}(\Delta m_\mathrm{f} + \Delta m_\mathrm{ox})} \tag{5}$$

where

$$I = \int_{t_0}^{t_b} F\, dt \tag{6}$$

$$\Delta m_{ox} = \int_{t_0}^{t_b} \dot{m}_{ox}\, dt \tag{7}$$

Specific impulse efficiency is defined by Eq. (8).

$$\eta_{I_{sp}} = \frac{I_{sp}}{I_{sp,\mathrm{th}}} \tag{8}$$

2.4.4. Density specific impulse

Equation (9) shows the calculation formula for the density specific impulse. In this calculation, the oxidizer density was taken as the liquid density of N_2O, 0.913 g/cm^3. The fuel density was calculated for each experiment by measuring the outer diameter, inner diameter, height, and mass of the fuel grain before combustion.

$$I_d = \frac{\rho_\mathrm{ox}\rho_\mathrm{f}\left(1 + \overline{O/F}\right)}{\rho_\mathrm{ox} + \left(\overline{O/F}\right)\rho_\mathrm{f}} \times I_{sp} \tag{9}$$

2.4.5. Mass utilization efficiency

Mass utilization efficiency is calculated using Eq. (10). This efficiency is defined as the ratio of the mass of expelled propellant to the mass of consumed propellant (fuel and oxidizer). As shown in Eq. (11), the mass of expelled propellant can be determined by subtracting the mass of combustion residue from the mass of consumed propellant.

The mass of combustion residue was determined from the mass difference of the entire combustion chamber assembly before and after combustion, rather than by directly scraping and measuring it from the aft combustion chamber. In this study, as illustrated in Fig. 12, the combustion chamber assembly refers to the combustion chamber, fuel, stainless steel plate, and gasket (O-ring).

$$\eta_\mathrm{u} = \frac{m_\mathrm{e}}{\Delta m_\mathrm{f} + \Delta m_\mathrm{ox}} \tag{10}$$

where

$$m_e = (\Delta m_f + \Delta m_{ox}) - m_{res} \tag{11}$$

2.4.6. Fuel regression rate

Equation (12) shows the calculation formula for the fuel regression rate. The inner diameter of the fuel grain at the end of combustion isn't necessarily perfectly circular, making accurate measurement with calipers difficult. However, since the overall combustion can be considered approximately uniform, this study assumed that the inner diameter burned uniformly inward. Therefore, the inner diameter of the fuel grain at the end of combustion was calculated from the difference in fuel mass before and after combustion.

$$\dot{r} = \frac{D_f - D_i}{2\Delta t} \tag{12}$$

$$D_f = \sqrt{\frac{4\Delta m_f}{\pi \rho_f L_f} + D_i^2} \tag{13}$$

3. Results

3.1. *C** efficiency

Figure 13 presents the results of the *C** efficiency evaluation. The top of the error bar indicates the maximum value, the bottom indicates the minimum value, and the plot represents the average value.

When the Mg additive ratio was 0 wt%, the *C** efficiency was $71.2 \pm 1.5\%$ for the L^* = 1.9 m combustion chamber and $78.7 \pm 4.8\%$ for the L^* = 3.7 m combustion chamber. The L^* = 3.7 m combustion chamber showed higher *C** efficiency compared to the L^* = 1.9 m combustion chamber. On the other hand, when Mg was added, the error bars overlapped in all combustion chambers, making it impossible to definitively state a significant difference.

Comparing the L^* = 1.9 m combustion chamber and the convergent nozzle combustion chamber, no significant difference in *C** efficiency was observed.

3.2. Mass utilization efficiency

Figure 14 shows the results of mass utilization efficiency evaluation. The top of the error bar represents the maximum value, the bottom represents the minimum value, and the plot is the average value. In all three combustion chamber geometries, mass utilization efficiency tends to decrease as the Mg additive ratio increases. This indicates a greater accumulation of combustion residue within the combustion chamber.

No significant difference in combustion residue expulsion was observed due to differences in nozzle geometry. At the maximum additive ratio of 40 wt% Mg, the value was 89.2 ± 1.0wt% for the rectangular nozzle combustion chamber and 98.0 ± 3.0wt% for the convergent nozzle combustion chamber.

On the other hand, a significant difference in combustion residue expulsion was observed due to differences in L^*. While there was no significant difference at 0 wt% and 20 wt% Mg, a notable difference in combustion residue percentage appeared at 40 wt% Mg, with 89.2 ± 0.1wt% for the L^* = 1.9 m combustion chamber and 94.1 ± 0.1wt% for the L^* = 3.7 m combustion chamber.

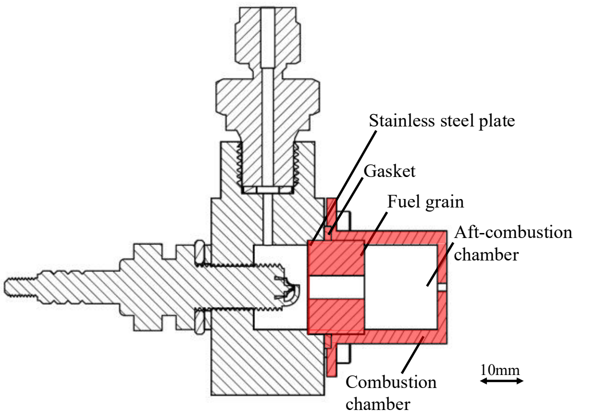

Fig. 12 . Mass measurement locations for combustion residue analysis.

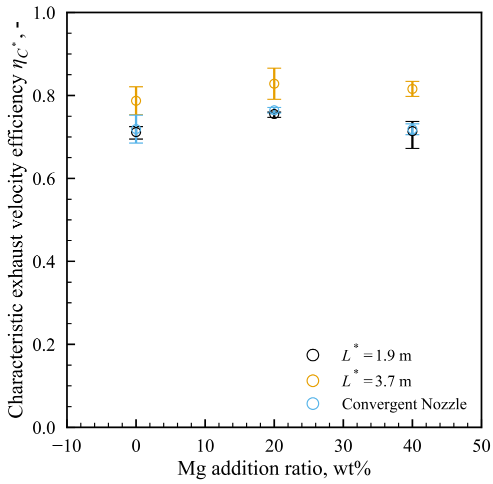

Fig. 13. *C** efficiency vs. Mg addition ratio.

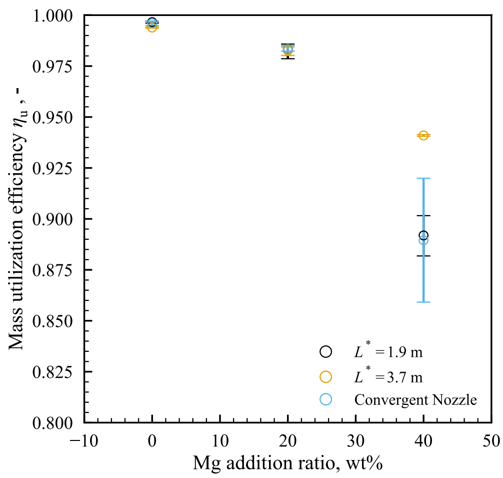

Fig. 14. Mass utilization efficiency vs. Mg addition ratio

3.3. Density specific impulse

Figure 15 shows the relationship between O/F ratio and density specific impulse for the three types of combustion chambers used in this study: L^* = 1.9 m, L^* = 3.7 m, and convergent nozzle. The NASA-CEA conditions were equilibrium flow, P_c = 0.4 MPa, and ε = 1. Focusing on the theoretical values, the peak density specific impulse for 0 wt%

Mg occurs at an O/F of 5-6, for 20 wt% Mg at 3-4, and for 40 wt% Mg at 2-3. Experimentally, 0 wt% Mg and 40 wt% Mg values are scattered around their optimal O/F, while 20 wt% Mg is slightly off from its optimal O/F.

To facilitate comparison of experimental results under each condition, Fig. 16 shows the relationship between the Mg additive ratio and density specific impulse. It's important to note that 20 wt% Mg is slightly off from its optimal O/F. From Fig. 16, particularly for the L^* = 1.9 m combustion chamber and convergent nozzle combustion chamber with 40 wt% Mg, the density specific impulse was remarkably lower compared to other conditions, with an average value of approximately 71.9 g·s/cm^3 for these four conditions. For the L^* = 3.7 m combustion chamber, the density specific impulse remained almost constant across all Mg additive ratios.

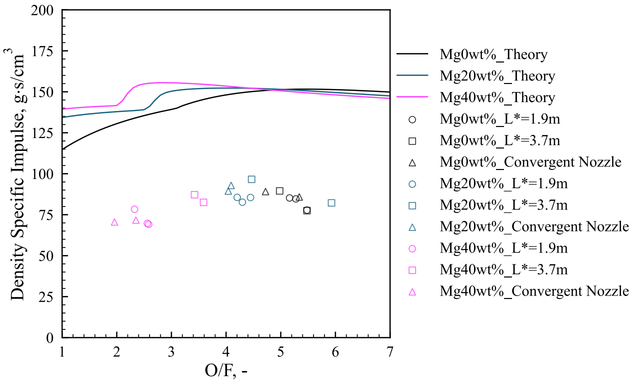

Fig. 15 Density specific impulse vs. O/F.

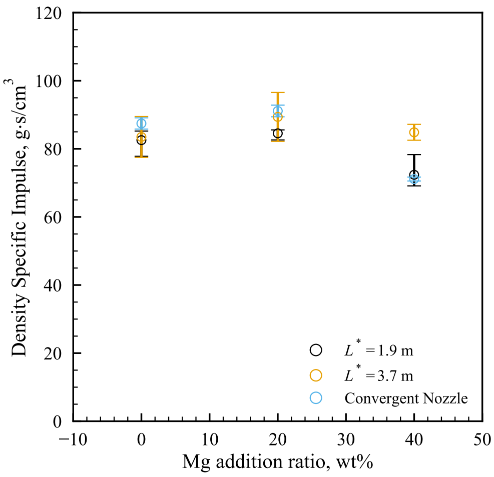

Fig. 16 Density specific impulse vs. Mg addition ratio.

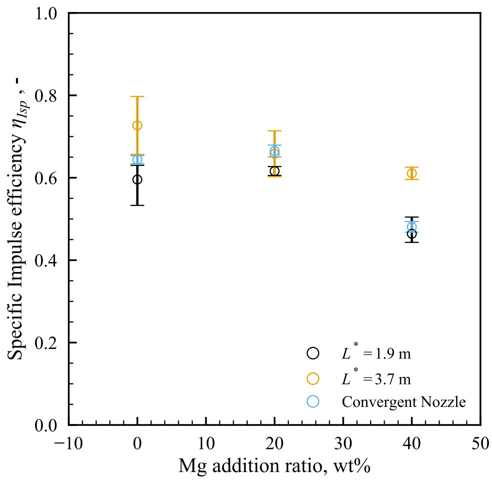

Fig. 17 Mg addition ratio vs. I_{sp} efficiency.

4. Discussion

4.1. Relationship between Nozzle Geometry and combustion residue percentage

The results from Section 3.2 indicated that the differences in nozzle geometry evaluated in this study didn't lead to a significant difference in combustion residue expulsion. We had expected that incorporating a convergent nozzle would improve gas flow within the combustion chamber and facilitate smoother residue expulsion; however, this effect wasn't clearly observed in practice.

On the other hand, when using fuel with 40 wt% Mg addition, a tendency was observed where the proportion of combustion residue decreased and mass utilization efficiency improved as L^* increased. From Fig. 14, it's not possible to determine whether more Mg was gasified, leading to a reduction in solid combustion residue itself, by using the L^* = 3.7 m combustion chamber. However, it can be inferred that the combustion residue was smoothly expelled when this combustion chamber was used.

The reason for this is presumed to be that the L^* = 3.7 m combustion chamber had a larger aft combustion chamber volume, providing more space to accumulate residue. As a result, the combustion residue did not densely accumulate immediately upstream of the nozzle, and obstruction of the nozzle flow path was suppressed, which is thought to have led to the smooth expulsion of the combustion residue.

This result suggests that, to reduce combustion residue in high Mg-loaded fuels, it is more important to ensure sufficient combustion chamber volume (i.e., a larger characteristic length combustion chamber) to provide adequate space for residue accumulation within the combustion chamber, rather than optimizing the nozzle shape.

4.2. Effect of Mg addition on density specific impulse

In Section 3.3, all three combustion chamber types showed no significant difference in density specific impulse for 0wt% and 20wt% Mg. However, density specific impulse tended to decrease, particularly in the L^* = 1.9 m combustion chamber and the convergent nozzle combustion chamber with 40wt% Mg. Theoretical calculations by NASA-CEA predicted that density specific impulse would improve as the Mg additive ratio to HTPB increased, but this trend was not necessarily confirmed by the experimental results. This indicates that despite an expected improvement in propellant energy density with Mg addition, its full effect was not realized. We will discuss the main reasons for this decrease in density specific impulse from the perspective of specific impulse and specific impulse efficiency.

Figure 17 shows the relationship between the Mg additive ratio and specific impulse efficiency. From this figure, it's clear that the specific impulse efficiency for the L^* = 1.9 m combustion chamber and convergent nozzle combustion chamber with 40 wt% Mg is remarkably low. As shown in Eq. (14), specific impulse efficiency is the product of C^* efficiency and nozzle efficiency. To analyze the factors contributing to the decrease in specific impulse efficiency in more detail, we'll examine the relationships of C^* efficiency and nozzle efficiency separately.

$$\eta_{I_{sp}} = \eta_{C^*} \times \eta_n \tag{14}$$

Figure 13 shows the relationship between Mg additive ratio and C^* efficiency, while Fig. 18 presents the relationship between Mg additive ratio and nozzle efficiency. From Fig. 18, it is evident that the nozzle efficiency of the L^* = 1.9 m combustion chamber and the convergent nozzle combustion chamber at 40 wt% Mg is clearly lower compared to the L^* = 3.7 m combustion chamber. This suggests that a significant decrease in nozzle efficiency is a primary factor leading to lower specific impulse efficiency.

The presence of combustion residue is a likely reason for the low nozzle efficiency under these conditions. As discussed in Section 3.2, an increase in the Mg additive ratio leads to an increase in combustion residue. Figure 14 confirms the generation of a large amount of residue, particularly in the L^* = 1.9 m combustion chamber and the convergent nozzle combustion chamber. It is highly probable that this large quantity of combustion residue accumulated densely in the aft combustion chamber, reducing the effective throat area and disrupting the flow within the nozzle. This likely resulted in a significant decrease in nozzle efficiency.

This indicates that to improve specific impulse and density specific impulse in hybrid rockets using Mg-added fuel, it is not enough to simply increase the Mg additive amount. It is also extremely important to consider the L^* and minimize the generation and expulsion of combustion residue, as well as their impact on nozzle performance.

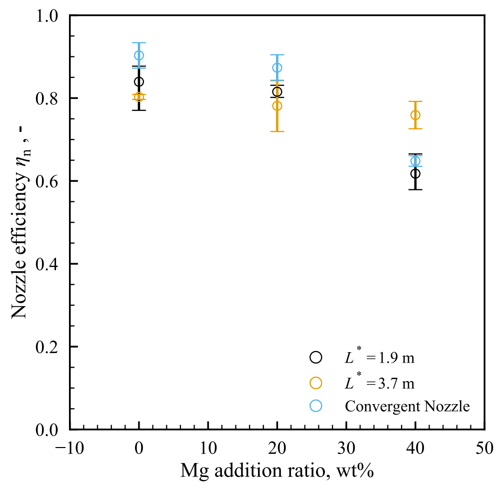

Fig. 18 Nozzle efficiency vs. Mg addition ratio

5. Conclusion

This study investigated combustion chamber design effects on a hybrid rocket using Mg-added HTPB fuel grain (0wt%, 20wt%, 40wt%) and N_2O, with three chamber types: rectangular nozzles (with characteristic length L^* of 1.9 m and 3.7 m) and a convergent nozzle (L^* = 1.9 m). Increasing L^* improved characteristic velocity (C^*) efficiency, regardless of Mg presence. Both Convergent and rectangular nozzles at L^* = 1.9 m yielded similar c efficiencies.

Combustion residue increased with Mg content. While nozzle geometry (rectangular vs. convergent) had no clear effect on residue expulsion, a longer L^* (3.7 m) significantly increased mass utilization efficiency at 40wt% Mg. This is likely due to increased aft-chamber volume , which provides more space for residue accumulation and thus mitigates nozzle blockage. Consequently, ensuring sufficient L^* is more crucial than optimizing nozzle shape for minimizing residue in high Mg-loaded fuel grains.

Experimental density specific impulse did not consistently align with theoretical predictions of improvement with increased Mg. A notable decrease occurred with L^* = 1.9 m and convergent nozzle chambers at 40wt% Mg. This performance drop is mainly attributed to a significantly reduced nozzle efficiency, likely caused by extensive residue accumulation in the aft-combustion chamber obstructing nozzle flow.

Therefore, to enhance performance in Mg-added hybrid thrusters, it is critical to consider L^* to effectively manage combustion residue generation and its impact on nozzle efficiency, rather than increasing the Mg content.

Acknowledgments

This work was supported by JSPS KAKENHI Grant Number JP24K17447.

References

1) Bryce Tech: Smallsats by the Numbers, 2023, https://brycetech.com/reports (accessed May 31, 2025).
2) Barato, F., Toson, E., Milza, F., & Pavarin, D.: Investigation of different strategies for access to space of small satellites on a defined LEO orbit, Acta Astronaut., 222 (2024), pp. 11–28.
3) Yuasa, S.: Characteristics of Ignition and Combustion of Metals, J. Combust. Soc. Jpn., 45 (2003), pp. 152–163.
4) Carmicino, C., & Sorge, A. R.: Experimental investigation into the effect of solid-fuel additives on hybrid rocket performance, Journal of Propulsion and Power, 31 (2015), pp. 699–713.
5) Gordon, S. and McBride, B. J.: Computer Program for Calculation of Complex Chemical Equilibrium Compositions and Applications, NASA Reference Publication1311, 1996.
6) Kanda, T., Nishii, K., and Kakami, A.: The relationship between the magnesium ratio in the grain and the performance of a hybrid rocket for spacecraft, 55th Annual Meeting of Japan Society for Aeronautical and Space Sciences, Tokyo, Japan, JSASS-2024-1045, 2024.